

Spin Texture Control and Magnetic Gap Engineering in a Ferromagnetic Insulator-Topological Insulator Sandwiched Heterostructure.

Mohammad T. H. Bhuiyan, Qile Li, James Blyth, Ji-Eun Lee, Jonathan Denlinger, Jaime Sánchez-Barriga, Alexander Fedorov, Anton Tadich, Emile Reinks, Sung-Kwan Mo, Alexei Fedorov, Oliver J. Clark, Mark T. Edmonds**

M. T. H. Bhuiyan, Q. Li, J. Blyth, O. J. Clark, M. T. Edmonds

School of Physics and Astronomy

Monash University

Clayton, VIC 3800, Australia

Email: oliver.clark1@monash.edu; mark.edmonds@monash.edu

M. T. H. Bhuiyan

Department of Physics

Pabna University of Science and Technology

Pabna 6600, Bangladesh

J. Blyth, M. T. Edmonds

ARC Centre for Future Low Energy Electronics Technologies

Monash University

Clayton, VIC 3800, Australia

Q. Li

Department of Chemistry

Stanford University

CA 94305, United States

A. Tadich

Australian Synchrotron, ANSTO

800 Blackburn Rd, Clayton VIC 3168, Australia

J. Lee, J. Denlinger, S. K. Mo, A. Fedorov

Advanced Light Source, LBNL

1 Cyclotron Road, Berkeley, CA 94720, United States

J. Sánchez-Barriga, E. Reinks, A. Fedorov

BESSY-II, Helmholtz Zentrum Berlin

Albert-Einstein-Straße 15, 12489 Berlin, Germany

Keywords: proximity magnetization, magnetic topological insulator, exchange gap, quantum anomalous Hall insulator, spin texture

Quantum materials combining magnetism and topological fermions are a key platform for low-energy electronics, spintronics, and quantum phases that break time-reversal symmetry (TRS), such as the quantum anomalous Hall effect (QAHE). Coupling a topological insulator to a magnetic material allows proximity magnetization with the potential to achieve these phases at elevated temperatures. One potential architecture for realizing QAHE at elevated temperature is a heterostructure comprising two single-septuple layers (1SL) of MnBi_2Te_4 (a 2D ferromagnetic insulator) with four-quintuple layer (4QL) Bi_2Te_3 in the middle. However, the origin of this gap has not yet been explicitly determined, as there are other non-magnetic mechanisms that have been shown to produce bandgaps in similar systems. Here, through spin- and angle-resolved photoemission, the magnetic nature of the gap opening is investigated to demonstrate direct control of the spin state via small magnetic fields and confirm the magnetic origin of the gap through spin splitting and broken TRS. Furthermore, the hallmark chiral spin texture of non-magnetic topological insulators is preserved away from the Γ -point, despite the large 72 ± 10 meV exchange gap at the Dirac point. The robust magnetic gap and controllable spin texture hold significant promise for future technologies requiring both magnetic properties and topological protection.

1. Introduction

Three-dimensional (3D) topological insulators (TIs) are a class of material with non-trivial band topology whose interior behaves as an insulator while its surface behaves as an electrical conductor. Due to a band inversion mediated by strong spin-orbit coupling, the surfaces of 3D TIs host spin-polarized massless Dirac cones.^[1] This spin polarization is predominantly locked in-plane and perpendicular to momentum and protected by time-reversal symmetry (TRS), resulting in a chiral spin texture^[2,3] as depicted in the left panel of **Figure 1a**. Inducing magnetic

order in an ultra-thin layer of a topological insulator is a powerful method for unlocking new topological phases, such as the quantum anomalous Hall effect (QAHE),^[2] where magnetism breaks time-reversal symmetry and opens an exchange gap, which hosts a chiral edge state within the gap depicted in the right panel of Figure 1a, that can support dissipation-less charge transport. This can be achieved in several ways, such as dilute magnetic doping of thin film TIs,^[4,5] intrinsic magnetic TIs,^[6,7] and proximity magnetization.^[8] Proximity magnetization - achieved by creating a heterostructure with a thin topological insulator film sandwiched between two ferromagnetic layers - represents one of the most effective strategies for achieving robust QAHE,^[9] as it isolates the magnetic layer from the TI layer, as shown in Figure 1b, which can significantly reduce magnetic disorder. The perpendicular magnetic anisotropy of the top and bottom ferromagnetic layers in such a heterostructure can significantly alter the surface state spin texture via proximity-induced uniform magnetic exchange interaction at the top and bottom surfaces.^[9-11] Here, the topologically non-trivial phase is retained, but the breaking of TRS opens a gap at the Dirac point (DP) of the surface states (SS), where electrons would be massless in the absence of magnetic order.^[8,12-15] Through explicit demonstration of the magnetic origin to the gap, one can infer the presence of a topologically-protected chiral edge mode, which has the potential to transport charge without loss.^[16]

A promising platform to explore proximity magnetization is with Bi_2Te_3 a topological insulator (TI) and MnBi_2Te_4 a magnetic topological insulator (MTI) that behaves as a ferromagnetic insulator in a single layer. Their similar structures and nearly identical lattice constants enable epitaxial growth of heterostructures, yielding unique electronic properties not found in either material alone. It has recently been experimentally demonstrated that 1SL MnBi_2Te_4 /4QL Bi_2Te_3 /1SL MnBi_2Te_4 (which we will refer to as MBT/4BT/MBT for the remainder of the article) is a promising ferromagnetic insulator-topological insulator heterostructure for realizing QAHE at higher temperatures, which exhibits a large exchange gap (75 meV) and relatively high Curie temperature (20-30 K).^[17] However, there is also evidence of gap opening in magnetic TIs driven by non-magnetic mechanisms such as MnBi_2Te_4 and $(\text{Bi}_{1-x}\text{Mn}_x)_2\text{Se}_3$ magnetic topological insulators.^[18,19] Therefore, it is crucial to confirm that the large exchange gap opening at the DP in the proximity coupled MBT/4BT/MBT is indeed of magnetic origin.

In this study, we demonstrate the epitaxial growth of a designer ferromagnetic insulator-topological insulator-ferromagnetic insulator (MBT/4BT/MBT) heterostructure. To verify the large exchange gap opening at the DP is magnetic in origin, we measure the spin-resolved electronic band structure using spin- and angle-resolved photoelectron spectroscopy (ARPES).

We then perform a comprehensive spin texture analysis of the heterostructure using spin-ARPES, an effective method to confirm TRS breaking and spin splitting, which underpin the magnetic origin of the exchange gap.^[2,20] Our study reveals that the large exchange gap of 72 ± 10 meV at the DP in the heterostructure originates from magnetic interactions. These measurements shed light on the spin texture in ferromagnetic-topological insulator sandwich heterostructures and provide insight into the role of TRS breaking on the exchange gap opening, and how the spin texture evolves at the exchange gap.

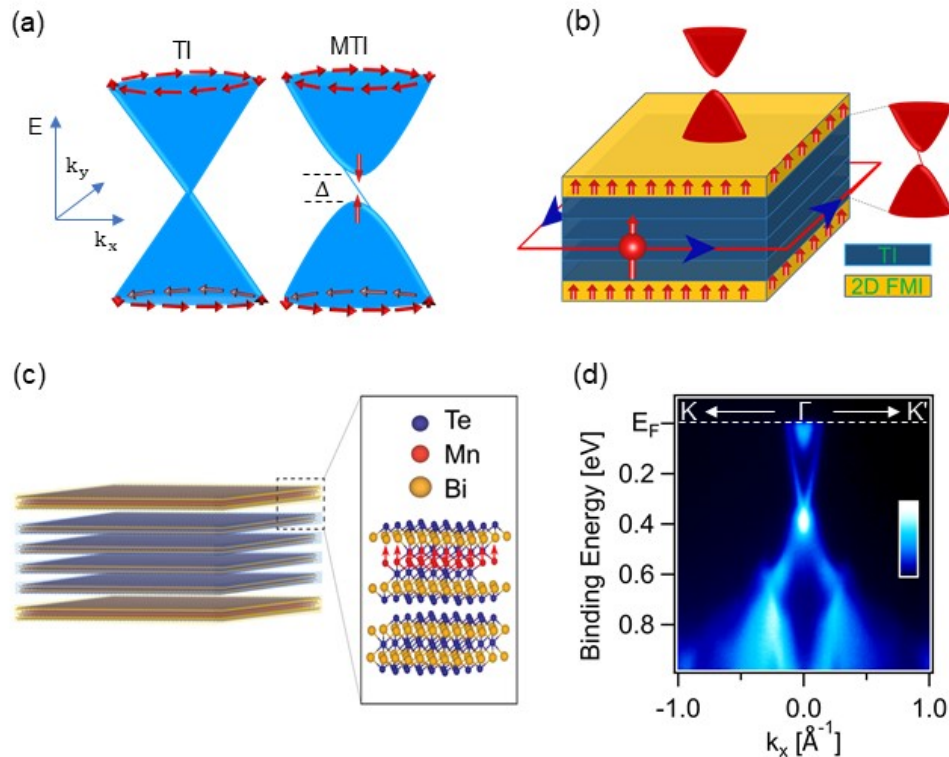


Figure 1. A ferromagnetic insulator–topological insulator heterostructure, 1SL MnBi_2Te_4 /4QL Bi_2Te_3 /1SL MnBi_2Te_4 . (a) Schematic band dispersion and spin textures of the surface states in TIs and magnetic TIs. (b) The magnetic exchange gap and spin-momentum locked chiral edge mode in a ferromagnetic insulator-topological insulator heterostructure. (c) Structure of the thin film heterostructure: four quintuple layers of Bi_2Te_3 between two single-septuple layers of MnBi_2Te_4 . Yellow sheets represent the ferromagnetic layers (MnBi_2Te_4), and blue sheets represent the topological insulator layers (Bi_2Te_3). Red arrows (inset) show the magnetic moments of Mn^{2+} in the MBT layer. (d) High-resolution ARPES spectra of the valence band along the $\text{K}\Gamma\text{K}'$ high-symmetry direction taken at 47 eV and $T= 13$ K.

2. Results and Discussion

Figure 1c shows the structural building block of the 1SL MnBi_2Te_4 -4QL Bi_2Te_3 -1SL MnBi_2Te_4 heterostructure. The atomic configurations in one quintuple Bi_2Te_3 and one septuple MnBi_2Te_4 layers are Te-Bi-Te-Bi-Te and Te-Bi-Te-Mn-Te-Bi-Te respectively. The origin of the magnetic properties in the MnBi_2Te_4 is the $3d$ states of Mn where the magnetic moment of the Mn atom is aligned with the out-of-plane easy axis.^[21]

High-quality MBT/4BT/MBT heterostructures were grown using molecular beam epitaxy (MBE) on Si(111) 7×7 substrates (see Methods for details). The reflection high-energy electron diffraction (RHEED) oscillations (see Figure S1b in the supplementary information) confirm the layer-by-layer growth of the heterostructure, whilst the sharp, bright streaks in the RHEED patterns in Figure S1c and S1d, supplementary information, indicate uniform surfaces and high crystallinity, confirming the high-quality epitaxial growth of our heterostructure. To characterize the electronic structure of the heterostructure, Figure 1d shows the valence band overview measured with ARPES at $T=13\text{K}$ (i.e., just below the Curie temperature) using a 47eV photon energy along the $\text{K}\Gamma\text{K}'$ high symmetry direction. The pronounced bright signal just below the Fermi energy (E_F) is the bulk conduction band whereas, the sharp, bright Dirac cone extending from the Fermi level to $\sim 0.32\text{ eV}$ binding energy corresponds to the SS electron bands which confirms the n -doped nature of the heterostructure. It is also evident that the DP region is above the bulk valence band region (BVB), which is different to, e.g., Bi_2Te_3 where the DP is situated within the BVB.^[17,22]

2.1. Energy Gap Determination by ARPES

Before examining the spin texture, we first use high-resolution ARPES to determine the size of the exchange gap in our heterostructure. The ARPES spectrum of the MBT/4BT/MBT heterostructure sample taken at 13K temperature with 47 eV and 42 eV photon energies along the $\text{K}\Gamma\text{K}'$ high symmetry direction is shown in Figure 2a and 2e respectively. These two photon energies were chosen as they highlight how the spectral weight of the surface states and Dirac point region are strongly photon energy dependent,^[23,24] and allow a complete overview of the system. In order to elucidate the band structure in further detail, especially the Dirac-like SS bands, we used the two-dimensional (2D) curvature analysis technique^[25] (Figure 2b and 2f) and energy dispersion curves (EDC) stack plotting (Figure 2c and 2g) technique.^[26,27] Figures 2b and 2f clearly capture the hyperbolic bands surrounding the gap region and demonstrate the band gap opening at the DP, but the non-physical band dispersion within the gap region is an artefact.^[28] This same band dispersion with finite mass gap is also evident from the EDC stack

plots extracted in Figures 2c and 2g. To precisely determine the gap size, we analyzed the EDC profile at the Γ -point using peak-fitting analysis, which is the most reliable and commonly used method for extracting exchange gaps from complex spectroscopic data—especially in cases where peaks are not well-defined or are overlapping.^[17,27,29] Figures 2d and 2h show the Γ -point EDC profiles from the 47 eV and 42 eV ARPES data, respectively that have been fit with Lorentzian peaks (after subtracting a Shirley background) to extract an exchange gap of 72 ± 10 meV (for detailed analysis, see supplementary information). This result is consistent with the gap size observed in both the 2D curvature analysis and the EDC stack plot. Importantly, the exchange gap size in our heterostructure is in good agreement with values reported in the literature for this heterostructure.^[17]

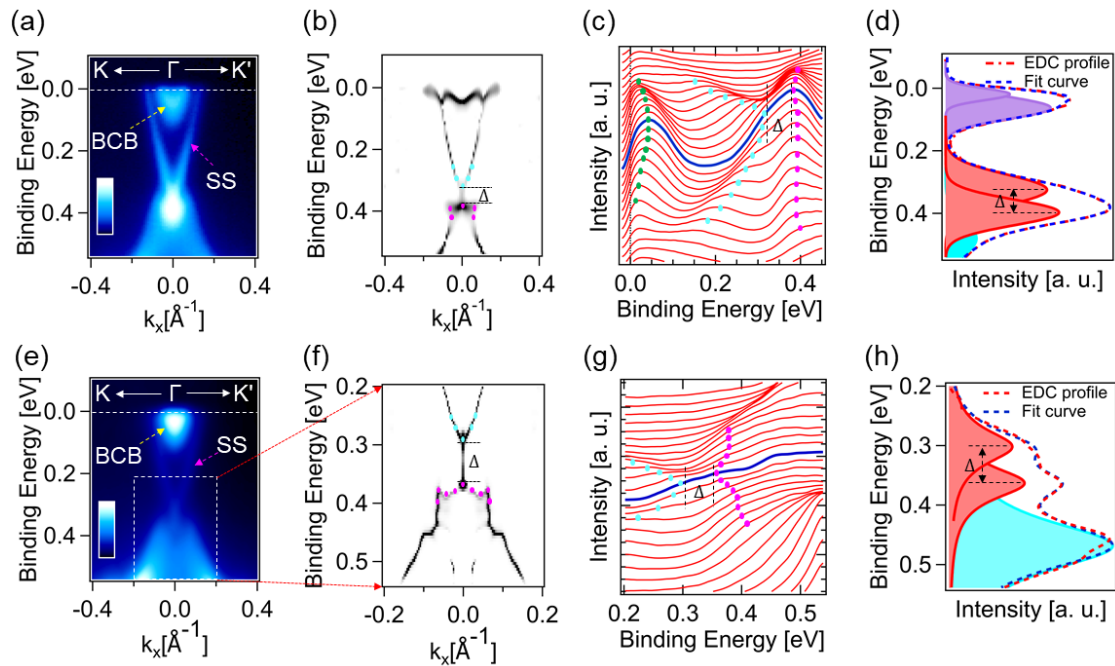


Figure 2. Determining the exchange gap of the MBT/4BT/MBT heterostructure. (a), (e) ARPES spectra taken at $T=13$ K along the $K\Gamma K'$ direction at $h\nu=47$ eV and $h\nu=42$ eV. (b), (f) Energy bands extracted from (a) and (e) via curvature analysis highlighting the SS conduction and valence bands. (c), (g) Stack plots of EDCs from (a) and (e), show peak positions of Dirac electron and hole bands (sky blue and pink dots) and bulk conduction bands (green dots). Blue solid lines indicate the Γ -point EDCs. (d), (h) Peak fitting results of EDC profiles at the Γ point from (a) and (e), where red-shaded regions represent SS electron and hole bands, and the violet and sky blue represent bulk conduction and valence bands respectively.

2.2. Spin Texture of Topological Surface States

To probe the nature of the observed mass gap and to characterise the full surface state spin texture, in Figure 3 we employ spin-ARPES, which is instrumental in probing the spin texture and TRS-breaking phenomena of the surface state, to investigate the magnetic origin of the gap opening at the DP in the MBT/4BT/MBT heterostructure. In order to obtain a complete picture of the spin texture of the surface states of a proximity-assisted magnetic topological insulator, we performed three-dimensional spin-resolved EDC measurements at Γ and at four further k-points symmetric about Γ , as indicated in Figure 3a and 3d with dashed lines. Asymmetry in the up and down spin profiles' intensity is obtained by, $A = (I_{up} - I_{down}) / (I_{up} + I_{down})$, and the spin polarization, shown in Figure 3b and 3(e), is obtained by, $P = A/S$, where $S=0.25$ is the Sherman function.

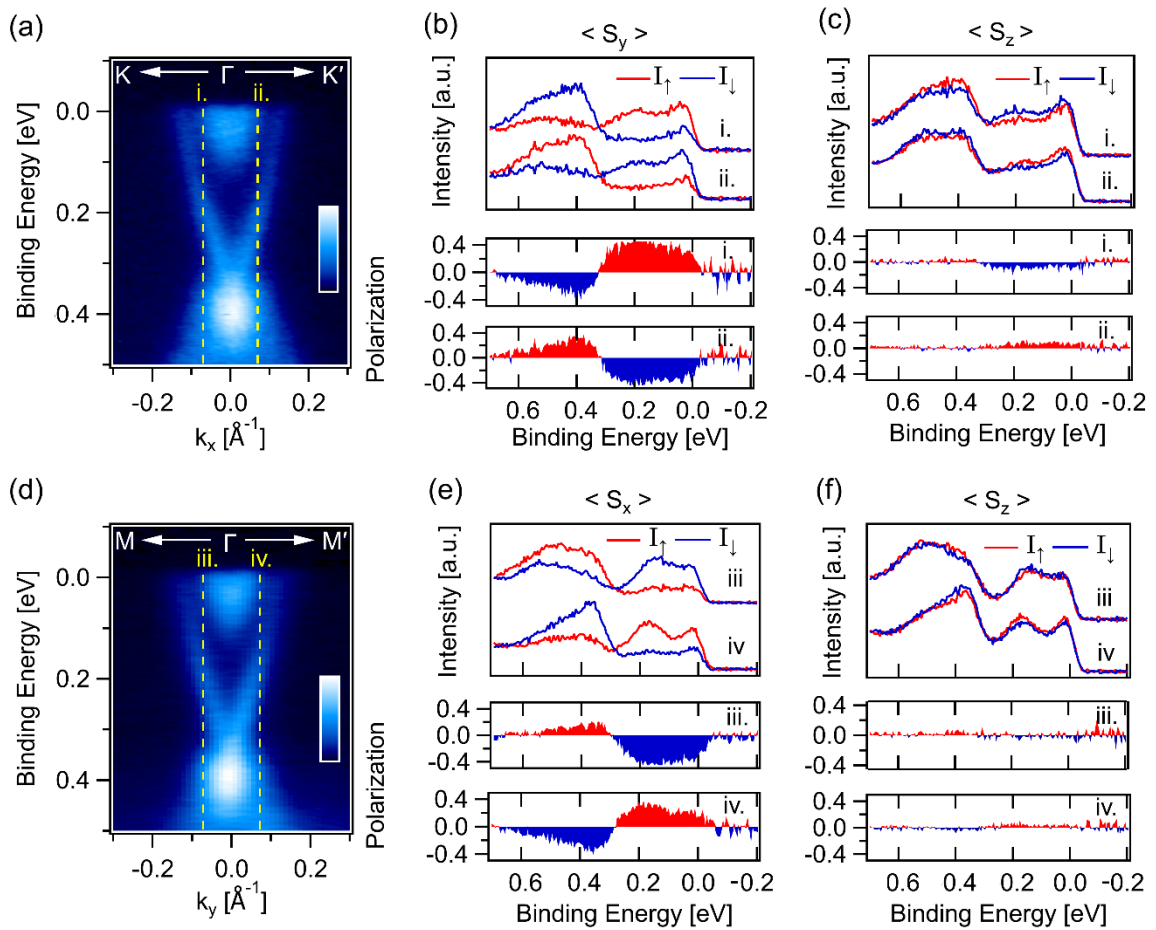


Figure 3. Spin texture of the MBT/4BT/MBT heterostructure away from the Γ -point. (a), (d) ARPES spectra along the $K\Gamma K'$ and $M\Gamma M'$ directions near the Brillouin zone center and Fermi surface. Yellow dashed lines indicate measurement positions for spin-resolved energy dispersion curves (EDC) shown in (b, c) and (e, f), corresponding to points (i), (ii), (iii), and (iv). (b), (c) Spin-resolved EDC and spin polarization (in-plane and out-of-plane) for positions

(i) and (ii). (e), (f) Spin-resolved EDC and spin polarization (in-plane and out-of-plane) for positions (iii) and (iv). Measurements were taken at $T=13\text{K}$ and $h\nu=47\text{ eV}$.

Lorentzian fits to the pairs of spin-EDCs at points (i) through (iv) demonstrate a predominantly chiral spin texture, with polarisation magnitudes of 71 ± 13 and $65\pm14\%$ above and below the DP along the $K\Gamma K'$ high symmetry cut. A similar chiral spin texture is also evident along the $M\Gamma M'$ direction with average polarisation magnitudes of 56 ± 17 and $59\pm18\%$ above and below the Dirac point respectively. While these in-plane spin polarisations are consistent with the TRS-protected universal chiral spin texture of the gapless surface state of topological insulators,^[2,30,31] a small spin polarization along the out-of-plane direction is also evident in Figures 3c and 3f. These signals also switch sign about $k_{\parallel}=0$, and thus arise from TRS-preserving mechanisms. This is consistent with the deviations to a fully chiral spin texture imposed by hexagonal warping of the constant-energy contours, as demonstrated in numerous non-magnetic TIs.^[11,32,33] While these measurements, therefore, do not demonstrate a magnetic component to the spin texture, we note that the probing light spot ($50\ \mu\text{m} \times 50\ \mu\text{m}$) is far larger than the magnetic domain size so is most likely probing multiple randomly oriented magnetic domains.^[24]

To bypass this issue, we pulse-magnetize our samples with a $\pm 0.5\text{ T}$ out-of-plane magnetic field (see methods) to align the domains during spin-ARPES measurements under remnant magnetization. This approach provides access to the magnetic spin component and also allows for the switching of the magnetic component of spin, thus offering unambiguous proof of its origin. We measured the out-of-plane spin profiles and corresponding polarization at the Γ -point, following oppositely oriented out-of-plane field pulses of $\sim 0.5\text{ T}$ at 27 eV and 6 K (well below the Curie temperature), as illustrated in Figures 4b and 4c. Despite both higher noise relative to the VLEED systems used for the data shown in Figure 3, and a preference for limited time-acquisitions to ensure the sample remained under remnant magnetization, Figures 4b and 4c clearly show significant spin asymmetry and polarization at the gapped DP, with the out-of-plane spin polarization flipping at the Γ -point as it crosses the Dirac gap (around 0.23 eV binding energy). More importantly, Figure 4c illustrates that the out-of-plane spin polarization reverses direction with the opposite polarity magnetization, confirming its magnetic origin. The presence of spin switching about the Dirac point is consistent only with the presence of a magnetic exchange gap, where spin-polarisation at $k=0$ is otherwise strictly enforced to be zero by TRS. This suggests the development of spin-splitting phenomena and breaking the Kramers' spin degeneracy ($E(k=0, \uparrow) \neq E(k=0, \downarrow)$) at the DP in the heterostructure.^[3,24] These findings

are consistent with the magnetic gap and spin-splitting observed in thick-films of Mn-doped Bi_2Te_3 .^[24] Furthermore, to be consistent with these findings, an out-of-plane spin-EDC taken at an elevated temperature of 45 K (well above the sample's Curie temperature), shown in Figure S3 in the supplementary information, demonstrates an absence of finite spin polarization, consistent with the lack of ferromagnetic order in the sample. These findings show that the band gap opening in MBT/4BT/MBT is magnetic in origin as a result of broken TRS. Finally, Figure 4d shows the iso-energy contour of our magnetic TI sample across the gap region, between the Fermi level and 0.50 eV. The red dashed lines represent the Dirac-like electron and hole bands, while the red and yellow arrows indicate the chiral in-plane spin texture, highlighting the opposite spin polarization of the electron-like and hole-like bands. Green arrows at the Dirac crossing show the spin orientation of the Dirac-like fermions at the Γ -point, which depends on the sample's magnetization order.

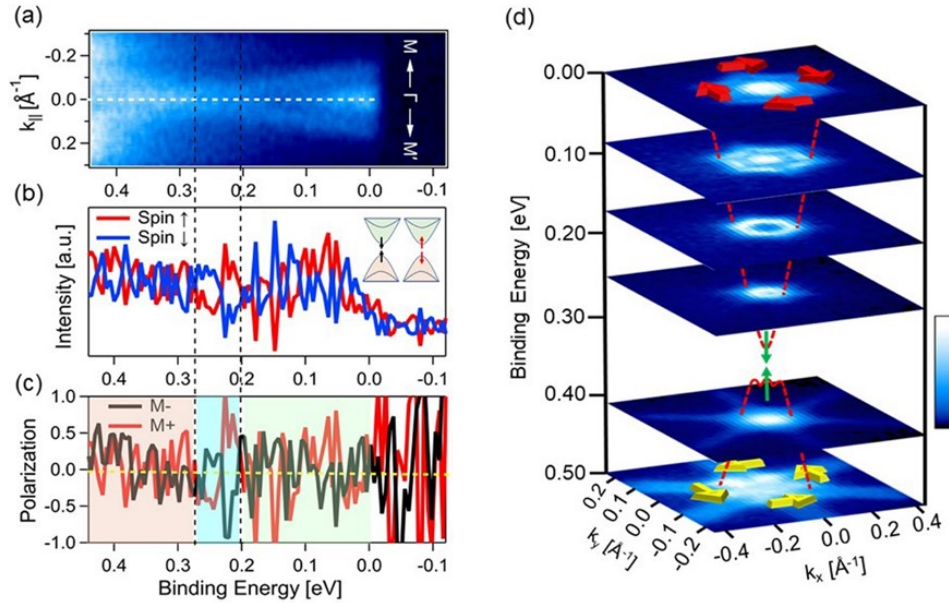


Figure 4. Confirming the magnetic origin of the gap. (a) Band dispersion of the heterostructure after magnetization, and the white dotted line indicate the spin measuring point in momentum space. (b) Γ -point spin profiles of the out-of-plane spin component, and spin alignments for M^- and M^+ polarity magnetizations (Inset). (c) Spin polarization at the Γ -point as a function of magnetization polarity: The blue shaded region represents the gapped Dirac crossing, and the green and brown shaded areas indicate the conduction and valence bands regions respectively. (d) Iso-energy contour of the heterostructure across the gap region with the spin-ARPES results. Red (yellow) arrows indicate the in-plane spin chirality of electrons (holes) away from the Γ -point, and the green arrows indicate the out-of-plane spin polarization at the gapped DP. Measurements were taken at $T = 6\text{K}$ and $h\nu = 27\text{ eV}$.

3. Conclusion

We have demonstrated that the MBT/4BT/MBT heterostructure exhibits a robust exchange gap of 72 ± 10 meV, significantly surpassing room temperature thermal broadening (25 meV). We have also demonstrated clear control of the magnetic spin state which reveals unambiguous evidence that the gap originates from magnetic interactions, whilst preserving the hallmark chiral spin texture of non-magnetic topological insulators away from the Γ -point. These findings provide important insights into the magnetic proximity effect in topological insulators and the delicate interplay between magnetism and non-trivial band topology. Furthermore, the ability to control the spin state with a modest 0.5 T pulse magnetic field makes magnetic-topological insulator heterostructures promising candidates for novel low-power spintronic device architectures and also paves the way for the advancement of lossless transport in topological insulators at higher temperatures.

4. Experimental Methods

Thin Film Heterostructure Growth: High-quality thin films of MBT/4BT/MBT were grown using molecular beam epitaxy (MBE) on *n*-type Si(111) 7x7 substrates at a growth temperature of 230°C under ultrahigh vacuum (UHV) conditions following an established recipe.^[17,27] High purity Mn (99.9%), Bi (99.999%), and Te (99.95%) source materials were used in the effusion cells to deposit them on the substrate during growth. Deposition rates were calibrated by a quartz crystal microbalance (QCM) prior to the growth process. Layer-by-layer epitaxial growth of the heterostructure was monitored and controlled via *in-situ* Reflection high-energy electron diffraction (RHEED). For beamline measurements at the Advanced Light Source (ALS), samples were grown in the MBE side chamber at the 10.0.1.1 endstation of ALS, with the pressure maintained below 8×10^{-10} mbar. For beamline measurements at BESSY-II Synchrotron, samples were grown using an Omicron Lab-10 MBE system at Monash University, with the pressure kept below 3×10^{-9} mbar. After growth, a 20 nm Tellurium capping layer was deposited to protect the films from contamination during transport to the spin-ARPES endstations at ALS and BESSY-II. After introduction into UHV, the tellurium capping layer was removed by mild-annealing prior to spin-ARPES measurements. The sample was gradually heated to a maximum temperature of 300 °C and held at this temperature for one hour to ensure the complete removal of the Te layer.

Electronic Structure and Spin-resolved Measurements: Spin-integrated electronic structure and spin-resolved measurements were carried out with *p*-polarized synchrotron light using the spin-ARPES on beamline 10.0.1.2 of the Advanced Light Source (ALS) at Lawrence Berkeley National Laboratory and beamline U125-PGM of the BESSY II Light Source at Helmholtz Zentrum Berlin. At ALS, data was taken using a Scienta-Omicron DA-30 spectrometer with two Ferrum VLEED detectors at 13 K (i.e., below the magnetic ordering temperature of 20 K). Measurements were carried out with two different photon energies (42 eV and 47 eV) to optimize the photoelectron signal. The spin-resolved energy dispersion curve (EDC) data was recorded along all three axes without moving the sample. Each spin-resolved EDC measurement was performed as a function of binding energy at a fixed momentum (*k*) with an energy resolution of 20 meV. The Sherman function value for the Ferrum VLEED detectors is 0.25. At BESSY II, the sample was pulsed magnetized with an *in-situ* 0.5 tesla magnet and data was taken using a Scienta R4000 spectrometer with two orthogonal Mott detectors. The spin-integrated ARPES spectra and the spin-resolved EDC were taken at 27 eV and T=6 K. The Sherman function value for the mini Mott detectors is 0.12.

Supporting Information:

Supporting Information is available from the Wiley Online Library or from the author.

Acknowledgements

M. T. E. acknowledges funding support from ARC Future Fellowship FT2201000290. M.T.E., and M. T. H. B., acknowledge funding support from ARC Discovery Project DP250100026. O.C., acknowledges funding support from ARC Discovery Project DP200101345. M.T.E., O.C., Q. L., and M. T. H. B. acknowledge travel funding provided by the International Synchrotron Access Program (ISAP) managed by the Australian Synchrotron, part of ANSTO, and funded by the Australian Government. This research used resources of the Advanced Light Source, which is a DOE Office of Science User Facility under contract no. DE-AC02-05CH11231. M. T. H. B. and J. B. acknowledge funding support from the AINSE postgraduate award.

References

- [1] Y. Xia, D. Qian, D. Hsieh, L. Wray, A. Pal, H. Lin, A. Bansil, D. Grauer, Y. S. Hor, R. J. Cava, M. Z. Hasan, *Nature Phys.* **2009**, 5, 398–402.

- [2] D. Hsieh, Y. Xia, D. Qian, L. Wray, J. Dil, F. Meier, J. Osterwalder, L. Patthey, J. Checkelsky, N. Ong, A. Fedorov, H. Lin, A. Bansil, D. Grauer, Y. Hor, R. Cava, M. Hasan, *Nature*. **2009**, 460, 1101–1105.
- [3] M. Z. Hasan, C. L. Kane, *Rev. Mod. Phys.* **2010**, 82, 3045.
- [4] Y. L. Chen, J. H. Chu, J. G. Analytis, Z. K. Liu, K. Igarashi, H. H. Kuo, X. L. Qi, S. K. Mo, R. G. Moore, D. H. Lu, M. Hashimoto, T. Sasagawa, S. C. Zhang, I. R. Fisher, Z. Hussain, Z. X. Shen, *Science* **2010**, 329, 659-662.
- [5] Y. Deng, Y. Yu, M. Z. Shi, Z. Guo, Z. Xu, J. Wang, X. H. Chen, Y. Zhang, *Science* **2020**, 367, 6480, 895-900.
- [6] Y. J. Chen, L. X. Xu, J. H. Li, Y. W. Li, H. Y. Wang, C. F. Zhang, H. Li, Y. Wu, A. J. Liang, C. Chen, S. W. Jung, C. Cacho, Y. H. Mao, S. Liu, M. X. Wang, Y. F. Guo, Y. Xu, Z. K. Liu, L. X. Yang, Y. L. Chen, *Phys. Rev. X* **2019**, 9, 4, 041040.
- [7] J. Li, Y. Li, S. Du, Z. Wang, B. Gu, S. Zhang, W. Duan, Y. Xu, *Sci. Adv.* **2019**, 5, eaaw5685.
- [8] F. Katmis, V. Lauter, F. S. Nogueira, B. A. Assaf, M. E. Jamer, P. Wei, B. Satpati, J. W. Freeland, I. Eremin, D. Heiman, P. Jarillo-Herrero, J. S. Moodera, *Nature*, **2016**, 533, 7604, 513–516.
- [9] S. Bhattacharyya, G. Akhgar, M. Gebert, J. Karel, M. T. Edmonds, M. S. Fuhrer, *Adv. Mater.* **2021**, 33, 2007795.
- [10] B. Karpiak, A. W. Cummings, K. Zollner, M. Vila, D. Khokhriakov, A. M. Hoque, A. Dankert, P. Svedlindh, J. Fabian, S. Roche, S. P. Dash, *2D Mater.* **2020**, 7, 015026.
- [11] L. Fu, *Phys. Rev. Lett.* **2009**, 103, 266801.
- [12] Z. Qiao, W. Ren, H. Chen, L. Bellaiche, Z. Zhang, A. MacDonald, Q. Niu, *Phys. Rev. Lett.* **2014**, 112, 116404.
- [13] Z. Qiao, S. A. Yang, W. Feng, W. Tse, J. Ding, Y. Yao, J. Wang, Q. Niu, *Phys. Rev. B*, **2010**, 82, 161414(R).
- [14] X. Qi, T. L. Hughes, S. Zhang, *Phys. Rev. B* **2008**, 78, 195424.

- [15] I. Garate, M. Franz, *Phys. Rev. Lett.*, **2010**, 104, 146802.
- [16] R. Yu, W. Zhang, H. Zhang, S. Zhang, X. Dai, Z. Fang, *Science* **2010**, 329, 5987, 61–64.
- [17] Q. Li, C. X. Trang, W. Wu, J. Hwang, D. Cortie, N. Medhekar, S.-K. Mo, S. A. Yang, M. T. Edmonds, *Adv. Mater.* **2022**, 34, 2107520.
- [18] S. H. Lee, Y. Zhu, Y. Wang, L. Miao, T. Pillsbury, H. Yi, S. Kempinger, J. Hu, C. A. Heikes, P. Quarterman, W. Ratcliff, J. A. Borchers, H. Zhang, X. Ke, D. Graf, N. Alem, C. -Z. Chang, N. Samarth, Z. Mao, *Phys. Rev. Res.* **2019**, 1, 012011.
- [19] J. Sánchez-Barriga, A. Varykhalov, G. Springholz, H. Steiner, R. Kirchschrager, G. Bauer, O. Caha, E. Schierle, E. Weschke, A. A. Ünal, S. Valencia, M. Dunst, J. Braun, H. Ebert, J. Minár, E. Golias, L. V. Yashina, A. Ney, V. Holý, O. Rader, *Nat. Commun.* **2016**, 7, 10559.
- [20] S. Y. Xu, M. Neupane, C. Liu, D. Zhang, A. Richardella, L. A. Wray, N. Alidoust, M. Leandersson, T. Balasubramanian, J. Sánchez-Barriga, O. Rader, G. Landolt, B. Slomski, J. H. Dil, J. Osterwalder, T. R. Chang, H. T. Jeng, H. Lin, A. Bansil, N. Samarth, M. Z. Hasan, *Nat. Phys.* **2012**, 8, 616–622.
- [21] P. Wang, J. Ge, J. Li, Y. Liu, Y. Xu, J. Wang, *The Innovation* **2021**, 2, 2, 100098.
- [22] Y. L. Chen, J. G. Analytis, J.-H. Chu, Z. K. Liu, S.-K. Mo, X. L. Qi, H. J. Zhang, D. H. Lu, X. Dai, Z. Fang, S. C. Zhang, I. R. Fisher, Z. Hussain, Z.-X. Shen, *Science* **2009**, 325, 5937, 178-181.
- [23] F. Kabir, M. M. Hosen, X. Ding, C. Lane, G. Dhakal, Y. Liu, K. Dimitri, C. Sims, S. Regmi, A. P. Sakhya, L. Persaud, J. E. Beetar, Y. Liu, M. Chini, A. K. Pathak, J.-X. Zhu, K. Gofryk, M. Neupane, *Front. Mater.* **2021**, 8, 706658.
- [24] E. D. L. Rienks, S. Wimmer, J. Sánchez-Barriga, O. Caha, P. S. Mandal, J. Růžička, A. Ney, H. Steiner, V. V. Volobuev, H. Groiss, M. Albu, G. Kothleitner, J. Michalička, S. A. Khan, J. Minár, H. Ebert, G. Bauer, F. Freyse, A. Varykhalov, O. Rader, G. Springholz, *Nature* **2019**, 576, 7787, 423–428.
- [25] P. Zhang, P. Richard, T. Qian, Y.-M. Xu, X. Dai, H. Ding, *Rev. Sci. Instrum.* **2011**, 82, 043712.

- [26] S. Y. Zhou, G.-H. Gweon, A. V. Fedorov, P. N. First, W. A. d. Heer, D.-H. Lee, F. Guinea, A. H. C. Neto and A. Lanzara, *Nat. Mater.* **2007**, 6, 770–775.
- [27] C. X. Trang, Q. Li, Y. Yin, J. Hwang, G. Akhgar, I. Di Bernardo, A. Grubišić-Čabo, A. Tadich, M. S. Fuhrer, S. K. Mo, N. V. Medhekar, M. T. Edmonds, *ACS nano* **2021**, 15, 8, 13444–13452.
- [28] P. Zhang, P. Richard, N. Xu, Y.-M. Xu, J. Ma, T. Qian, A. V. Fedorov, J. D. Denlinger, G. D. Gu, H. Ding, *Appl. Phys. Lett.* **2014**, 105, 172601.
- [29] Y. L. Chen, J.-H. Chu, J. G. Analytis, Z. K. Liu, K. Igarashi, H.-H. Kuo, X. L. Qi, S. K. Mo, R. G. Moore, D. H. Lu, M. Hashimoto, T. Sasagawa, S. C. Zhang, I. R. Fisher, Z. Hussain, Z. X. Shen, *Science* **2010**, 329, 5992, 659-662.
- [30] Z.-H. Pan, E. Vescovo, A. V. Fedorov, D. Gardner, Y. S. Lee, S. Chu, G. D. Gu, T. Valla, *Phys. Rev. Lett.* **2011**, 106, 257004.
- [31] C. Jozwiak, Y. L. Chen, A. V. Fedorov, J. G. Analytis, C. R. Rotundu, A. K. Schmid, J. D. Denlinger, Y.-D. Chuang, D.-H. Lee, I. R. Fisher, R. J. Birgeneau, Z.-X. Shen, Z. Hussain, A. Lanzara, *Phys. Rev. B.* **2011**, 84, 165113.
- [32] S. Souma, K. Kosaka, T. Sato, M. Komatsu, A. Takayama, T. Takahashi, M. Kriener, K. Segawa, Y. Ando, *Phys. Rev. Lett.* **2011**, 106, 216803.
- [33] Z. Alpichshev, J. G. Analytis, J.-H. Chu, I. R. Fisher, Y. L. Chen, Z. X. Shen, A. Fang, A. Kapitulnik, *Phys. Rev. Lett.* **2010**, 104, 016401.

Supporting Information

Spin Texture Control and Magnetic Gap Engineering in a Ferromagnetic Insulator-Topological Insulator Sandwiched Heterostructure.

Mohammad T. H. Bhuiyan, Qile Li, James Blyth, Ji-Eun Lee, Jonathan Denlinger, Jaime Sánchez-Barriga, Alexander Fedorov, Anton Tadich, Emile Reinks, Sung-Kwan Mo, Alexei Fedorov, Oliver J. Clark, Mark T. Edmonds**

Table of contents

- 1. Layer-by-layer Growth of MBT/4BT/MBT Heterostructure**
- 2. Energy Gap Determination by ARPES**
- 3. Spin Polarization at High Temperature**

1. Layer-by-layer Growth of MBT/4BT/MBT Heterostructure

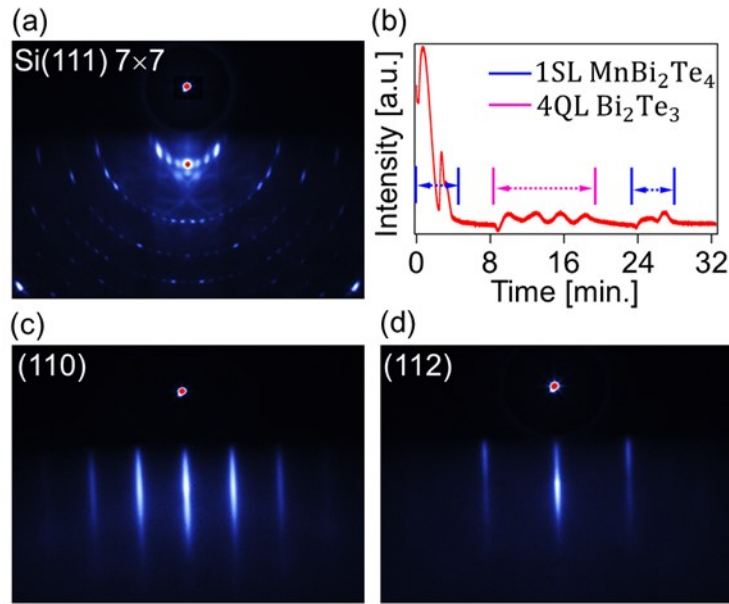


Figure S1. RHEED images of the substrate and the heterostructure. (a) RHEED pattern of Si(111) 7×7 surface reconstruction just before the heterostructure growth. (b) RHEED oscillations for layer-by-layer growth of MBT/4BT/MBT heterostructure. Blue and pink colours indicate the growth time for Bi₂Te₃ and MnBi₂Te₄ layers. (c) and (d) RHEED patterns of the heterostructure taken at the end of the growth along the (110) and (112) azimuths.

2. Energy Gap Determination by ARPES

We subtract a Shirley background before performing the EDC profile analysis. EDC profiles in Figure S2(a) manifest two distinct peaks at 0.05 eV and 0.38 eV, where the second peak is apparent to be asymmetric and might be comprised of two or three different peaks and requires peak fitting analysis to confirm it. We fit this profile with five individual Lorentzian line shapes. The first two peaks, just below the Fermi level (shaded violet), correspond to the bulk conduction bands. The third and fourth peaks at 0.325 eV and 0.397 eV (shaded in red) correspond to the SS conduction and valence bands respectively resulting in an exchange gap of 72 ± 10 meV. The fifth peak at 0.48 eV (shaded sky blue) corresponds to the bulk valence band. In addition to this, the EDC profiles in Figure S2(b) show three distinct peaks at 0.30 eV, 0.38 eV, and 0.47 eV. We fit this profile with three individual Lorentzian line shapes. The first and second peak near the DP, located at 0.300 eV and 0.365 eV respectively, corresponds to surface state conduction and valence bands. This peak splitting in the EDC spectra confirms the exchange gap of 65 ± 12 meV. The third peak at 0.468 eV (shaded sky blue) corresponds to the bulk valence band. The calculated exchange gap sizes for the 42 eV and 47 eV data are

found to be well consistent with the apparent gap size in the 2D curvature and EDC stack plot images. More importantly, the exchange gap size confirmed in our heterostructure agrees well with the existing literature.^[17]

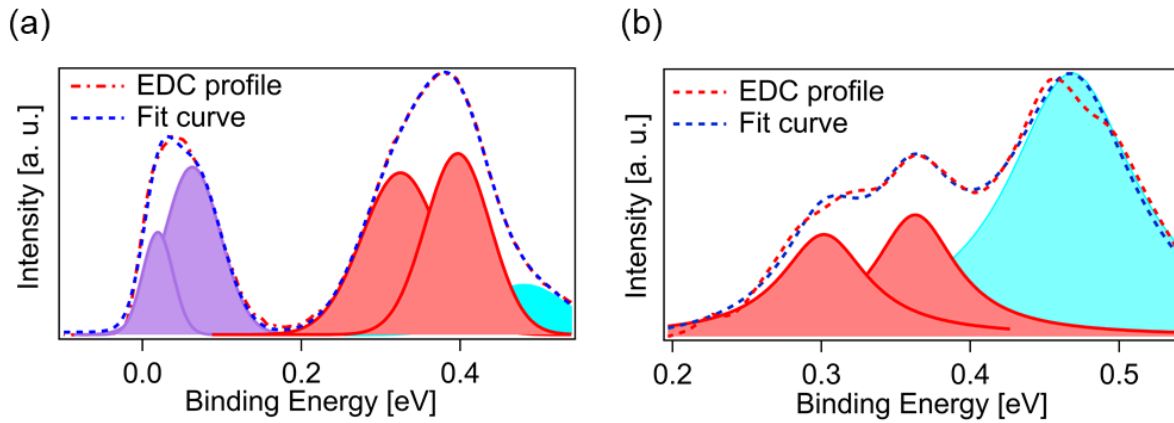


Figure S2. Peak fitting analysis of Γ -point EDC profiles. (a) taken at 47 eV and (b) at 42 eV where red-shaded regions represent SS electron and hole bands, and the violet and sky blue represent bulk conduction and valence bands respectively.

3. Spin Polarization at High Temperature

In order to prove the magnetic origin of the exchange gap opening at the Dirac point we measured the out-of-plane spin polarization at the Γ -point at elevated temperature ($T=45\text{K}$, well above the Curie temperature), which is shown in Figure S3. Our high temperature spin data reveals that the out-of-plane spin asymmetry and the spin splitting feature at the Dirac point region vanishes as the heterostructure sample becomes paramagnetic at elevated temperature.

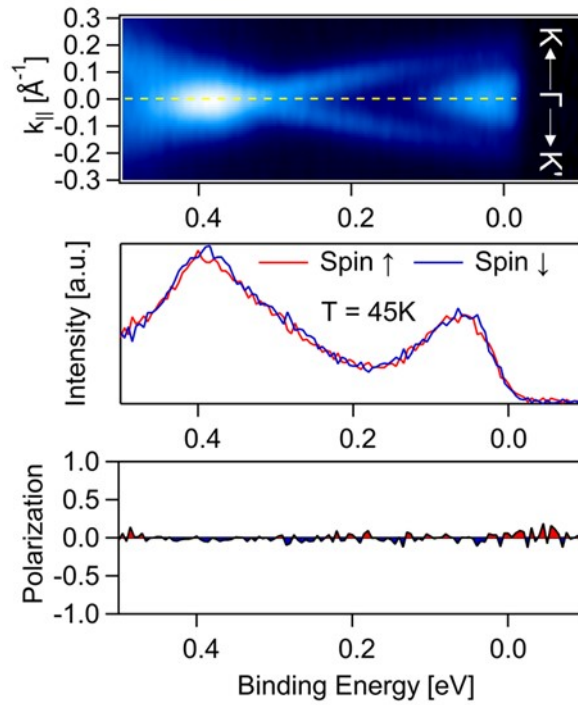


Figure S3. Out-of-plane spin polarization at the Γ -point at elevated temperature. The top panel shows the band dispersion taken at 47 eV where the yellow dotted line indicates the spin measuring point in the momentum space. The middle panel illustrates the out-of-plane spin components at the Γ -point at elevated temperature ($T=45\text{K}$) where the red and blue color lines represent the up-spin and down-spin profiles respectively. The bottom panel indicates the corresponding out-of-plane spin polarization.